JGR Atmospheres

RESEARCH ARTICLE
10.1029/2021JD035197

Special Section:
Using radiative-convective equilibrium to understand convective organization, clouds, and tropical climate

Key Points:

- Global tropical cyclone (TC) count decreases while intensity and size increase with surface warming in radiative-convective equilibrium simulations
- Most of the TC precipitation comes from extreme rates which become more extreme with surface warming
- Sea surface temperature (SST) and TC intensity dominate precipitation metric change while impacts of size are metric-dependent

Supporting Information:

Supporting Information may be found in the online version of this article.

Correspondence to:
A. M. Stansfield,
alyssa.stansfield@stonybrook.edu

Citation:
Stansfield, A. M., & Reed, K. A. (2021). Tropical cyclone precipitation response to surface warming in aquaplanet simulations with uniform thermal forcing. *Journal of Geophysical Research: Atmospheres*, *126*, e2021JD035197. https://doi.org/10.1029/2021JD035197

Received 4 MAY 2021
Accepted 2 DEC 2021

Tropical Cyclone Precipitation Response to Surface Warming in Aquaplanet Simulations With Uniform Thermal Forcing

Alyssa M. Stansfield[1] and **Kevin A. Reed**[1]

[1]School of Marine and Atmospheric Sciences, Stony Brook University, Stony Brook, NY, USA

Abstract While many modeling studies have attempted to estimate how tropical cyclone (TC) precipitation is impacted by climate change, the multitude of analysis techniques and methodologies have resulted in varying conclusions. Simplified models may be able to help overcome this problem. Radiative-convective equilibrium (RCE) model simulations have been used in various configurations to study fundamental aspects of Earth's climate. While many RCE modeling studies have focused on TC genesis, intensification, and size, limited work has been done using RCE to study TC precipitation. In this study, the response of TC precipitation to sea surface temperature (SST) change is analyzed in global Community Atmosphere Model (CAM) aquaplanet simulations run with Radiative-Convective Equilibrium Model Intercomparison Project protocols, with the addition of planetary rotation. We expect that the insight gained about how TC precipitation responds to SST warming will help predict how TCs in the real world respond to climate change. In the CAM RCE simulations, the warmer SST simulations have less TCs on average, but the TCs tend to be larger in outer size and more intense. As simulation SST increases, more extreme precipitation rates occur within TCs, and more of the TC precipitation comes from these extreme rates. For extreme (99th percentile) TC precipitation, SST, and TC intensity increases dominate the 8.6% per K increase, while TC outer size changes have little impact. For accumulated TC precipitation, SST, and TC intensity contributions are still the majority, but TC outer size changes also contribute to the 6.6% per K increase.

1. Introduction

Precipitation from tropical cyclones (TCs) can create dangerous hazards, such as flash floods and landslides, and cause expensive damages to personal property and infrastructure; therefore, it is important to understand how TC precipitation is affected by climate change. Observations by the Tropical Rainfall Measuring Mission and the Global Precipitation Measurement mission from 1998 to 2016 show an increasing trend in global average TC precipitation of about 1.3% per year, resulting in a 21% increase for 0.21°C of warming over the 19 year period (Guzman & Jiang, 2021). Various studies have attributed extreme precipitation amounts from Hurricanes Harvey, Florence, and Dorian to anthropogenic climate change (K. A. Emanuel, 2017; Reed et al., 2020, 2021; Risser & Wehner, 2017; Trenberth et al., 2018; Van Oldenborgh et al., 2017; Wang et al., 2018) while others have estimated how much TC precipitation may increase due to climate warming in the future (Gutmann et al., 2018; Kim et al., 2014; Knutson et al., 2013, 2015; Liu et al., 2018, 2019; Patricola & Wehner, 2018; Stansfield, Reed, & Zarzycki, 2020; Villarini et al., 2014; Wehner et al., 2015; Wright et al., 2015). All of these studies use different methodologies, models, warming scenarios, precipitation metrics, and TC tracking algorithms, and while some focus on specific ocean basins or overland regions, others consider TCs all over the globe. With all of these differences, the quantitative conclusions about TC precipitation increases vary. A recent summary assessment (Knutson et al., 2020) estimated a 14% (with a range of 6%–22%) increase in global mean near-storm TC precipitation rates for 2°C warming, which is in line with the theoretical Clausius-Clapeyron (C-C) rate of about 7% per 1°C warming. While some studies project increases around the C-C rate (e.g., Knutson et al., 2015; Villarini et al., 2014), others estimate TC precipitation increases exceeding the C-C (e.g., Liu et al., 2018; Patricola & Wehner, 2018; Wehner et al., 2015; Wright et al., 2015), potentially due to increases in average TC intensity due to climate warming (Liu et al., 2019). Quantifying TC precipitation change is complicated and influenced by particular choices of model parameters and details of the analysis. In such cases, simplified models can bypass technical details and help reveal the fundamental physical processes of interest.

Radiative-convective equilibrium (RCE) is an idealized representation of the tropical atmosphere, where radiative cooling is statistically balanced by latent heat release and surface heat fluxes. Traditional non-rotating RCE model simulations, with uniform thermodynamic forcing spanning domains of various sizes, have been used to study various aspects of tropical meteorology and climate, including convective self-aggregation (e.g., Bretherton et al., 2005; Wing & Cronin, 2016; Wing et al., 2017), changes in extreme precipitation due to warming (e.g., Muller, 2013; Muller et al., 2011; Pendergrass et al., 2016; Romps, 2011), and the response of convection and clouds to warming (e.g., Cronin & Wing, 2017; Seeley & Romps, 2015; Tompkins & Craig, 1999). When RCE simulations include rotation, TCs spontaneously develop. TC genesis, intensification, and structure have been studied using a variety of RCE model configurations, including small, f-plane domains that contain single TCs (e.g., Carstens & Wing, 2020; Knutson & Tuleya, 2004; Nolan et al., 2007; Ramsay et al., 2020; Wing et al., 2016) and larger domain simulations with multiple TCs (e.g., Chavas & Emanuel, 2014; Held & Zhao, 2008; Zhou et al., 2014). However, these model configurations simulate TCs on a flat, cartesian surface and therefore do not include the impacts of Earth's spherical geometry on TCs, namely the beta effect (Chan, 2005; Merlis & Held, 2019).

An intermediary between limited-domain RCE model simulations and realistic Earth-like general circulation model (GCM) simulations is an aquaplanet configured GCM in a RCE state. This configuration creates a theoretical world that has been used to study climate sensitivity (Popke et al., 2013), the impact of model parameters on convection (Reed, Medeiros, et al., 2015), and the response of clouds to warming (Bony et al., 2016). Adding rotation to these GCM simulations creates a so-called "TC world" that can be used to study fundamental TC characteristics and behaviors in a simplified setting. In this set-up, TCs can exist anywhere in the domain due to the lack of land and globally uniform warm sea surface temperatures (SSTs). Shi and Bretherton (2014) provided a description of the general climate and large-scale dynamics of this type of simulation and observed that most TCs generate in the subtropics, move westward and poleward due to beta drift, and end up at high latitudes near the poles, where multiple TCs exist at any one time and may interact with each other. This configuration deviates from traditional RCE set-ups (Merlis & Held, 2019), but Reed and Chavas (2015) demonstrated that a global "TC world" with a constant Coriolis parameter (f) has similar properties to limited-area f-plane RCE simulations. In the simulations for this study, the planetary rotation rate is set to the same value as Earth (i.e., f is not constant and the TCs are impacted by beta drift). For simplicity, we will refer to our simulations as RCE simulations.

Since the pioneering research of Shi and Bretherton (2014), subsequent studies have tested the sensitivity of the TCs in these "TC worlds" to changes in environmental forcings. Merlis et al. (2016) investigated the response of TC counts and intensities to changes in the globally uniform SST. They found that with increasing SST, the time mean global number of TCs decreases, the region of persistent TC activity moves poleward, and the median TC intensity increases. While these shifts in TC characteristics were due to changes in their thermodynamic environment, Chavas and Reed (2019) explored dynamical controls on TC genesis and outer size by altering the planetary radius and rotation rate. In their simulations, TC genesis rates increase moving away from the equator, peak at a critical latitude, and then decrease moving poleward. TC outer size generally increases slowly as the storms move toward the poles until they reach a transition latitude, which is poleward of the peak genesis latitude, and then gradually decrease in size. Walsh et al. (2020) studied the response of TC genesis to different large-scale climate conditions using simulations with varying globally uniform SSTs and with imposed meridional SST gradients. Overall, they found that the strongest control on TC genesis was vertical static stability, and in their simulations with constant SSTs, the number of TCs decreased with warmer SSTs, in agreement with Merlis et al. (2016). Hsieh et al. (2020) used slightly altered "TC worlds," with cold SST caps at the poles to avoid the aggregation of TCs there, to explore the transition of convective clusters into rotating TC precursors and how this transition depends on planetary rotation rate, planetary radius, and SST. This study found a small, non-monotonic dependence of the transition probability in the tropics on SST, which they related to changes in the large-scale low-level vorticity associated with the weak meridional overturning circulation.

While it is not always obvious how well results from RCE simulations apply to real-world TCs, Chavas et al. (2017) suggests that the TC structure in RCE simulations, realistic Earth-like simulations, and observations are consistent. Additionally, Chavas and Reed (2019) showed that the slow increase in TC outer size with latitude in the lower mid-latitudes in their RCE simulations was similar to behavior found in a historical Earth-like simulation using the same model, which is also qualitatively consistent with observations (Chavas et al., 2016). With that in mind, RCE simulations have some advantages over Earth-like GCM simulations. Because RCE simulations involve a world with uniform thermodymamic forcing, including constant SSTs and insolation, and without land, they provide a simple test case for examining fundamental forcings and feedbacks with TCs and their environments and also within TCs themselves. This allows us to focus on the TCs specifically and their responses to forcing changes in the model, without interactions with cold SSTs, strong wind shear, and land that normally weaken or terminate TCs in realistic simulations. As a result of these conditions, this type of simulation produces many more TCs per year than the real Earth and therefore is ideal for studying the statistical properties of TC structure. Another advantage of RCE simulations is that they require less computational resources than Earth-like GCM simulations and therefore can be run with higher spatial resolutions needed to investigate phenomenon like TCs (Reed, Bacmeister, et al., 2015; Reed & Jablonowski, 2012; Shaevitz et al., 2014; Wehner et al., 2014).

To the authors' knowledge, no work has yet been done to closely examine TC precipitation in "TC world" simulations. Exploring how TC precipitation in these idealized simulations responds to increasing SSTs may help understand how real-world TCs will respond to climate change. To this end, this work will quantify changes in TC precipitation, as well as other TC characteristics that can impact precipitation such as intensity and outer size, in RCE "TC world" simulations with varying globally uniform SSTs. Section 2 describes the model set-up, TC tracking and precipitation extraction methodology, and TC precipitation analysis framework. Section 3.1 presents results about TC characteristics including occurrences, genesis counts, outer sizes, and intensities and compares these results to previous "TC world" studies. Section 3.2 describes results concerning TC precipitation changes. Section 4 is a discussion of the overall conclusions, implications of the results, and directions for future work.

2. Model Description and Analysis Methodology

2.1. RCE Model Configuration

The model used for this study is the Community Atmosphere Model (CAM), version 5 (Neale et al., 2012). CAM is the atmospheric component of the Community Earth System Model version 2 (CESM2; Danabasoglu et al., 2020), a comprehensive fully coupled global climate model that is part of the Coupled Model Intercomparison Project (CMIP; Eyring et al., 2016). Specifically, CAM's spectral element dynamical core (Dennis et al., 2012; Lauritzen et al., 2018; Taylor & Fournier, 2010; Taylor et al., 1997) is utilized with the default physical parameterization packages (Neale et al., 2012). The horizontal grid spacing is approximately 28 km over the entire global domain. CAM at TC-permitting resolutions has been shown to reproduce realistic TC genesis and track patterns (Bacmeister et al., 2018; Reed, Bacmeister, et al., 2015; Wehner et al., 2014; Zarzycki & Jablonowski, 2014), radial wind profiles (Chavas et al., 2017; Reed & Chavas, 2015), and precipitation (Stansfield, Reed, Zarzycki, Ullrich et al., 2020; Villarini et al., 2014).

The model is run in a RCE configuration, following the protocols of the Radiative-Convective Equilibrium Model Intercomparison Project (RCEMIP; Wing et al., 2018; Wing et al., 2020), which established a standardized configuration for RCE simulations to facilitate comparison between models and establish a baseline for future studies. For these experiments, every model gridpoint experiences the same incident solar radiation at all times, so there are no diurnal or seasonal variations in insolation. The solar constant is set to 551.58 W m^{-2} while the solar zenith angle is set to 42.05°, which results in an insolation of 409.6 W m^{-2}, the annual mean value in the tropics (20°S–20°N). The concentrations of most atmospheric trace gases are also set to globally uniform values. More details about the RCEMIP protocols for geophysical constants, radiation parameters, and initialization procedures can be found in Wing et al. (2018). Similar CAM RCE configurations have been used in multiple recent TC studies (Chavas & Reed, 2019; Chavas et al., 2017; Reed & Chavas, 2015; Reed, Medeiros, et al., 2015). The only difference in the model set-up used for this study from the set-up described in Wing et al. (2018) and in the initial results discussion in Wing et al. (2020) is that rotation is included by setting the planetary rotation rate of the model to the value of Earth's planetary rotation rate (7.292115×10^{-5} s^{-1}). By including rotation, f is not a constant. Each simulation is run for 2 years, and the first two months are discarded to allow for spin-up. To examine the spin-up, we plot the time evolution of the change in global mean precipitation between each 3-hourly timestep and the next timestep (see Figure S1 in Supporting Information S1). When the 30-day running mean of this value goes to zero, we consider the simulation spun-up. This occurs for all simulations around day 60 after initialization.

SSTs are constant in time and space, and each simulation has a different globally uniform SST ranging from 295 to 305 K in 1 K increments, resulting in a total of 11 simulations. This range was chosen based on SSTs under real-world TCs. Global TC tracks for 1981–2019 were obtained from the International Best Track Archive for Climate Stewardship (IBTrACS; Knapp et al., 2010). The NOAA daily Optimum Interpolation Sea Surface Temperature (OISST) data set provided the SSTs at 0.25° resolution (Banzon et al., 2016). Only the SSTs nearest

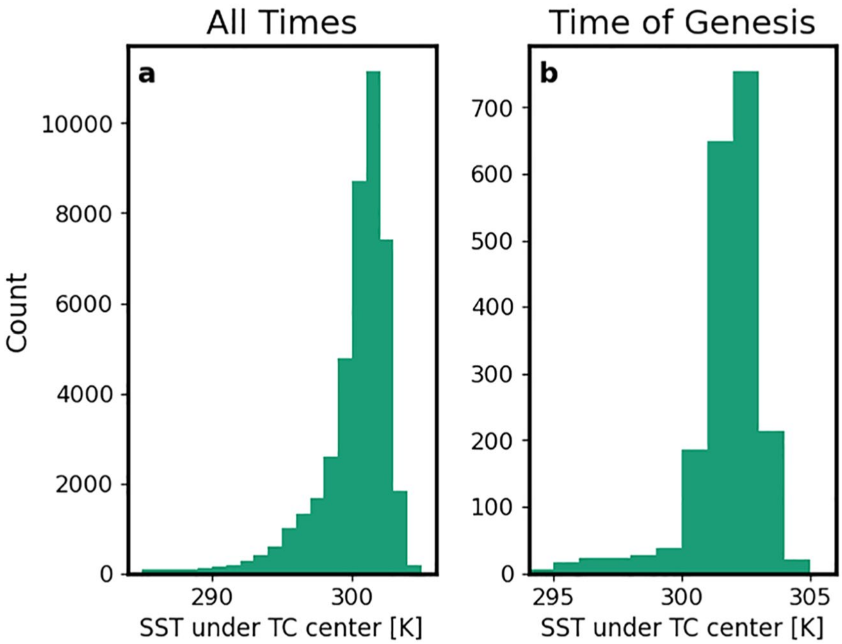

Figure 1. Histograms of sea surface temperature (SSTs) in K under observed tropical cyclone (TC) centers for (a) all times in the TCs' lifetimes and (b) at the time of TC genesis. Observed TC tracks for 1981–2019 are obtained from the IBTrACS data set, and SSTs are from the NOAA Optimum Interpolation Sea Surface Temperature data set. Only TCs with maximum wind speeds above 18 m s^{-1} are included. The data are binned into 1 K intervals.

to the TCs' center locations are included, and TCs are only included if their maximum wind speed in IBTrACS equals or exceeds 35 kt (18 m s^{-1}), which is the Saffir-Simpson scale definition of a tropical storm. As shown in Figure 1a, about 94% of the SSTs under TCs are in the range 293–303 K, with the cooler SSTs likely from when TCs moved over extratropical ocean water. Looking at the SSTs at the times of TC genesis, the majority (91%) of TCs form over SSTs between 300 and 304 K (Figure 1b). We chose the SST range of 295–305 K for our model simulations to best match the range of SSTs observed under TCs in the real-world.

2.2. TC Tracking and Precipitation Extraction

The open-source TempestExtremes software package (Ullrich & Zarzycki, 2017; Ullrich et al., 2021) is used to detect and track TCs in the native model output (cubed sphere grid), as well as extract TC-related precipitation based on dynamic estimates of the TCs' sizes. First, potential TCs are identified at each 3-hourly model time step based on locations of sea level pressure (SLP) minima and retained if there's an increase in SLP of at least 4 hPa within 5° great-circle distance from each SLP minimum. This checks for a closed SLP contour around the SLP minimum. The potential TC candidates are then stitched together into TC tracks based on their spatial proximity, but for a track to be recorded, the TC must exist for at least 48 hr and have a maximum wind speed of at least 17 m s^{-1} for at least 4 model time steps (12 hr). For each TC at every time in its lifetime, an azimuthal-mean radial wind profile is calculated, and from that profile, the radius of the 8 m s^{-1} wind, outside the radius of maximum wind, is identified. This radius is the measure of the TC's outer size, and all precipitation within it is extracted as the TC-related precipitation. This process is very similar to the TC tracking used in Stansfield, Reed, Zarzycki, Ullrich et al. (2020), although there are some differences in the definition of TCs due to the differences in the simulations. For example, the potential TC candidate identification in Stansfield, Reed, Zarzycki, Ullrich et al. (2020) included a search for warm-core cyclone characteristics and the TC track stitching step included a minimum latitude limit, since those model simulations included extratropical cyclones. Because RCE simulations don't produce extratropical cyclones, the tracking parameters can be more lenient. The TempestExtremes tracking parameters used for this study are similar to those used in Reed and Chavas (2015).

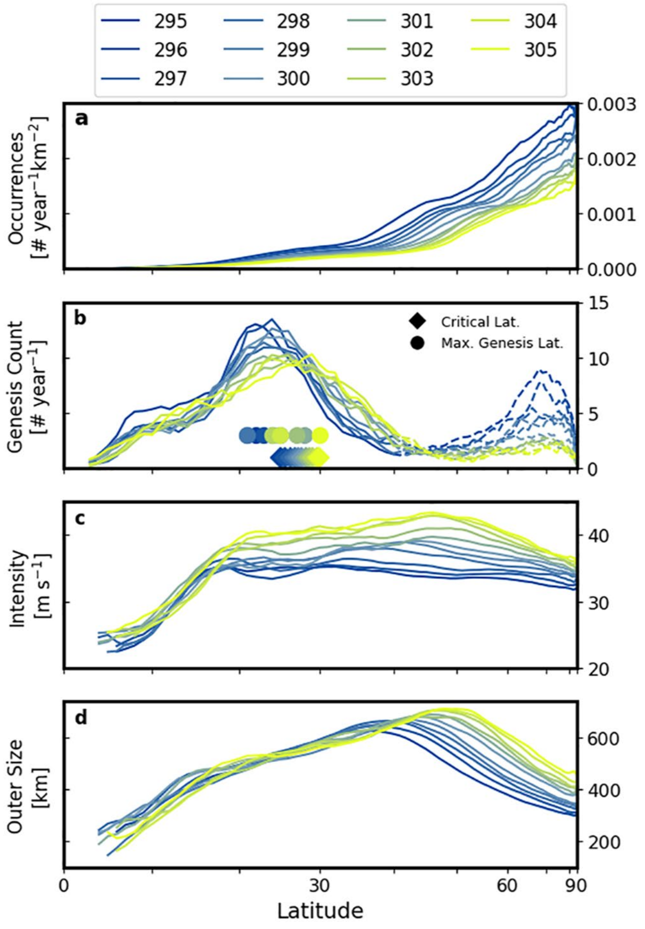

Figure 2. Zonal mean (a) area-weighted tropical cyclone (TC) occurrences (# year^{-1} km^{-2}), (b) TC genesis counts (# year^{-1}), (c) TC intensities (m s^{-1}), and (d) TC outer sizes (km). The occurrences and genesis counts are annual means. The legend at the top shows the SST of each simulation. The data are binned into 1° latitude bins from 90°S to 90°N, averaged over both hemispheres, and then smoothed using a moving average with a window width of 5°. The diamond markers above the *x*-axis of plot b show the values of the critical latitude for each simulation, while the circle markers show the latitude of maximum genesis count.

2.3. TC Precipitation Analysis Methods

To compare TC precipitation among the different model simulations and on a common spatial grid, composites of TC precipitation are calculated using the NodeFileCompose algorithm within TempestExtremes (Ullrich et al., 2021). NodeFileCompose takes the TC precipitation at each 3-hourly output time in each TC's lifetime, maps it onto an equidistant cartesian stereographic projection centered on the detected TC center point, and then averages all the TC precipitation “snapshots” together to create a composite. The horizontal grid spacing of the stereographic grid is 0.25° in both the *x* and *y* directions. More details about the mathematical operations used to create the composite grid projections can be found in Ullrich et al. (2021).

To look at TC precipitation in a different way, we also create precipitation frequency and amount distributions modeled after those in Figure 1 of Pendergrass and Hartmann (2014). The logarithmically distributed precipitation rate bins described in Pendergrass and Hartmann (2014) are utilized to adequately sample the entire precipitation rate spectrum within TCs from very light to very extreme precipitation. In log coordinates, each precipitation rate bin is 7% wider than the previous bin and has a bin center that is 7% larger than the previous bin center. All non-zero TC precipitation rates are included in the distributions. To calculate the frequency distributions, a TC precipitation histogram is created at each gridpoint using the extracted TC precipitation described in Section 2.2 and then normalized by the total number of 3-hourly timesteps. For the amount distributions, the amount of TC precipitation that comes from each precipitation bin is added up at each gridpoint. Finally, the area-weighted means of the frequency and amount distributions are calculated from all gridpoints to get the global-mean distributions. For more details about the bin and distribution calculations, see Pendergrass and Hartmann (2014).

3. Results

3.1. TC Occurrences, Intensities, and Outer Sizes

3.1.1. Analysis of TC Occurrences and Spatial Characteristics

Before analyzing TC precipitation, we first explore other TC characteristics, such as genesis location, global coverage, size, and intensity, because these will impact precipitation per TC (size and intensity) and TC contribution to global precipitation (genesis location and global coverage). Understanding how these characteristics change with SST will help explain the response of TC precipitation to SST change in Section 3.2. Since the thermodynamic forcing in these model simulations is uniform everywhere, zonal and hemispheric means are reasonable estimations of global TC behavior. Figure 2a shows the annual mean zonal mean TC occurrences, normalized by the area within the 1° latitude bin intervals.

This area-weighting accounts for the decrease in surface area with increasing latitude. This plot demonstrates that in all of the simulations, TCs tend to accumulate near the poles, as shown by the maximum TC occurrences at 90°, which was also observed in previous studies (Chavas & Reed, 2019; Merlis et al., 2016; Shi & Bretherton, 2014; Walsh et al., 2020). At all latitudes, the cooler simulations have higher TC occurrences than the warmer simulations, suggesting that there are less TCs overall in the warmer simulations. This conclusion is consistent with Merlis et al. (2016) and Walsh et al. (2020), even though these two studies used different models with different forcings and resolutions than the simulations discussed here. This suggests that the physical mechanisms causing the decrease in TC occurrences with warmer SSTs are ubiquitous in global RCE simulations. Walsh et al. (2020) found that the magnitudes of the zonal mean atmospheric lapse rates decreased (i.e., became less negative) in their simulations with warmer SSTs and suggested that this increase in atmospheric stability led to the decrease in TC genesis. In our simulations, the magnitude of the zonal mean lapse rate also decreases as SST increases (Figure S2 in Supporting Information S1). Hsieh et al. (2020) examined the transitions of TC seeds to TCs in a hierarchy of models and found that the probability of this transition is inversely proportional to the ventilation index (described in Tang and Emanuel (2012)). In our simulations, the zonal mean ventilation index increases with warmer SSTs (Figure S2 in Supporting Information S1), suggesting that TC seeds may have a harder time transitioning into TCs in the warmer simulations.

Figure 2b shows the annual mean zonal mean TC genesis counts. All simulations have peak genesis between 20° and 30° latitude (see circle markers above the *x*-axis), but this peak generally shifts poleward and decreases in magnitude in the warmer simulations, which is the same pattern seen in Merlis et al. (2016). Between about 30° and 45°, the genesis counts in the warmer simulations are larger than the cooler simulations, suggesting that TCs tend to form further poleward with warmer SSTs. Chavas and Reed (2019) found in their "TC world" experiments that the latitude of maximum TC genesis is similar to the critical latitude, which is a transition latitude that separates the wave-dominated equatorial belt and the TC-dominated polar cap. The critical latitude is determined in part by a velocity scale that is estimated by the TC potential intensity (PI; K. A. Emanuel, 1999), which is the theoretical maximum intensity a TC can attain in a given environment. Since the PI increases as SST increases (see Figure S3 in Supporting Information S1 for a plot of zonal mean PI), the critical latitude also increases (see the diamond markers above the *x*-axis of Figure 2b). The poleward shift of the latitudes of maximum genesis counts for the warmer simulations is consistent with this poleward shift of the critical latitudes. There is a secondary genesis peak for most of the simulations around 70°, but this peak is in part an artifact of the TC tracker momentarily "losing" TCs when they get too weak near the poles and then re-tracking them again when they get stronger or merge with another TC. To avoid any complications from these weakening and merging TCs in the precipitation analysis, we exclude TCs poleward of 40° from the TC precipitation analysis, notated by the dashed lines in Figure 2b. Justification for using 40° is discussed later in this section.

Figure 2c shows the zonal mean TC intensity, as measured by the 3-hourly maximum wind speed in the 2D low-level wind field. Equatorward of about 20°, the mean intensities are very similar for all the simulations. Since TCs are typically forming at these latitudes (Figure 2b) they are, on average, in the development phase of their life cycles and not intense in these regions. Therefore, the mean TC intensity tends to be the same regardless of SST. Poleward of 20°, the mean intensity increases as the SST increases. This is in agreement with PI theory, as higher SST results in higher PI. The mean intensity is lower than the PI at all latitudes (Figure S3 in Supporting Information S1), showing that the average TC in these model simulations does not come close to its theoretical PI.

Figure 2d shows the zonal mean TC outer size, measured by the radius of the 8 m s^{-1} wind outside the radius of maximum wind. For all simulations, the mean outer size tends to increase from the equator to a point between 40° and 50° latitude and then decrease from there to the poles, which is consistent with the behavior seen in Chavas and Reed (2019). The mean outer size appears to be relatively insensitive to model SST from the equator to about 40°. This suggests that TC outer sizes in the real tropics will not change with global SST warming. However, in Earth-like model simulations, many studies (Bacmeister et al., 2018; Kim et al., 2014; Stansfield, Reed, & Zarzycki, 2020; Sun et al., 2017; Wehner et al., 2018) project TC outer size increases due to climate change; therefore these outer size increases are likely driven by factors other than global SST increase with climate change, such as changes in SSTs near the TCs compared to the tropical mean SST (Chavas et al., 2016; Lin et al., 2015).

Poleward of 40°, the model simulations diverge on their behavior, with the mean outer TC size starting to decrease more equatorward in the cooler simulations while in the warmer simulations, the TCs continue to grow in size and don't begin decreasing in size until closer to the poles. Therefore, mean TC outer size tends to be larger in the warmer simulations than the cooler simulations near the poles. This could be a result of the TCs having more space to fill, since there are less TCs near the poles in the warmer simulations (Figure 2a). As described in Chavas and Reed (2019), between the equator and the critical latitude TC outer size is limited by the Rhines scale, which is not dependent on SST. Between the critical latitude, which moves slightly poleward as SST increases (diamond markers in Figure 2b), and the poles, TC outer size is limited by an inverse-f scale that is proportional to a velocity scale, which for TCs is estimated as the PI. Since PI increases as SST increases as discussed above, the inverse-f scale is larger at the same latitude for a warmer SST simulation compared to a cooler SST simulation, and therefore the mean TC outer size can be larger as well.

To further investigate the spatial TC characteristics, Figure 3 shows time mean TC counts (green diamonds), TC outer sizes (orange circles), and TC spatial coverages (purple triangles). Filled markers represent values

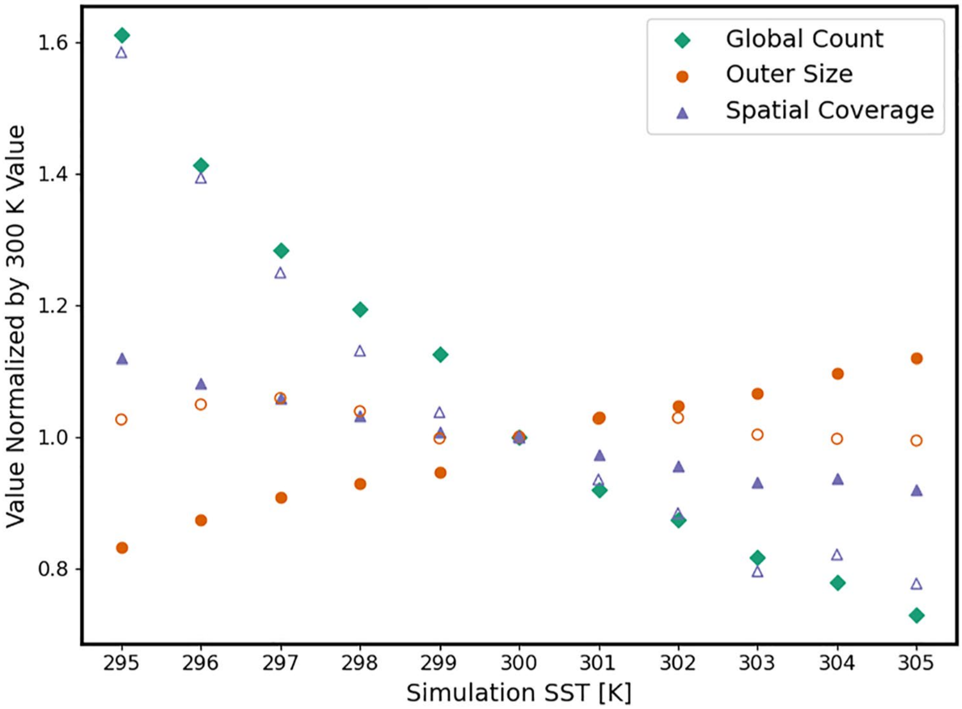

Figure 3. Time mean tropical cyclone (TC) count (green diamonds), TC outer size (orange circles), and TC spatial coverage (purple triangles). The *x*-axis shows the SSTs of the model simulations. All values are normalized by the 300 K simulation values. Filled markers represent values calculated using TCs over the entire globe, while unfilled markers represent values calculated only using TCs equatorward of 40°. For reference, the 300 K value of count is 83.5 storms, outer size is 519.2 km, and spatial coverage is 15.7% for the whole globe, and for 40–40°, the 300 K outer size is 555.1 km and spatial coverage is 4.3%.

calculated using TCs over the entire globe, while unfilled markers represent values calculated using TCs that are equatorward of 40°. The cutoff of 40° is chosen because we want to exclude the TCs that merge or die and re-form near the poles, and 40° is a point of very low genesis for all the simulations (see Figure 2b). Additionally, 40° is the latitude where the zonal mean outer sizes start to diverge in behavior, and equatorward of 40° is where the mean outer sizes are all similar in Figure 2d. As a sensitivity test, we also performed all of the analysis using 50° as the cutoff latitude, since 50° is poleward of all the latitudes of minimum genesis, and the main results discussed for throughout the rest of Section 3 remain the same. In Figure 3, all of the values are normalized by the 300 K simulation values (which are listed in the figure caption) so that the different variables can be shown on the same *y*-axis.

While the TC counts monotonically decrease by about 7.0 TCs per K increase in SST (consistent with Figure 2a), TC outer size increases by about 14.8 km per K. Note that these slopes are calculated using the non-normalized values (not shown).

These results suggest that the warmer simulations have less TCs at any one time, but the TCs are, on average, larger. Based on Figure 2d, the differences in outer sizes between simulations are mainly driven by the TCs poleward of about 40°. This is consistent with the unfilled outer size markers, as they show a slight decrease of 2.7 km per K. Since TC counts and outer sizes vary inversely, the mean spatial coverage of TCs is plotted in Figure 3 to see which change dominates. The spatial coverage is defined as the time mean percentage of the globe covered by TCs for the filled triangle markers and the time mean percentage of the area between 40°S and 40°N covered by TCs for the unfilled triangle markers. The global spatial coverage decreases as simulation SST increases by about 0.3% per K, but not as drastically as the TC counts decrease, showing how the increasing TC outer sizes offset the decreasing counts. The 40–40° spatial coverage also decreases as simulation SST warms by about 0.3% per K.

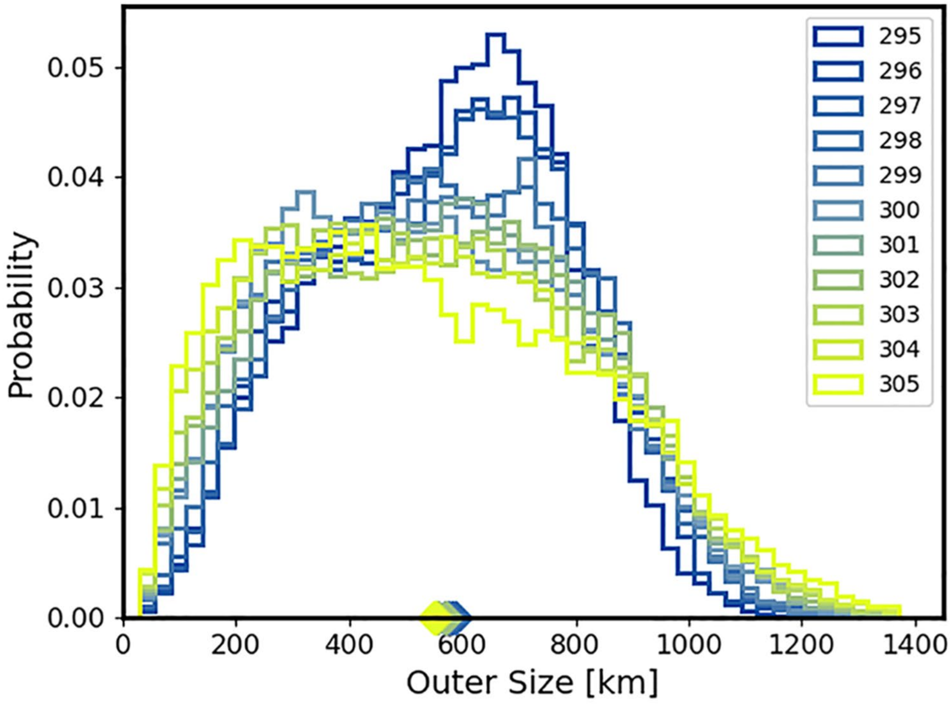

Figure 4. Normalized distributions of tropical cyclone (TC) outer sizes (km) for all simulations. Only times when the TCs are equatorward of 40° are included. The diamond markers on the *x*-axis show the means of the distributions.

3.1.2. Distributions of TC Intensity and Outer Size

To further examine the variability in TC outer sizes and the potential impact on TC precipitation, we plotted in Figure 4 the normalized distributions of TC outer sizes for each simulation, but only for TCs equatorward of 40° to exclude TCs that form near the poles due to tracker specifications (see Figure 2b). As the simulation SST increases, the distributions get wider and have less of a distinct peak, while the means of the distributions (diamond markers on *x*-axis) decrease slightly, with all values just under 600 km. This is consistent with Figure 2d, since the mean outer size for all simulations is similar until about 40°. Note that the outer size distributions for all TCs with no latitude limit (not shown) show a clear increase in mean outer size as SST increases. The slight decrease in mean outer size and the flattening of the distributions as the SST increases in Figure 4 is likely due to the differences in peak genesis latitude. Since the TCs tend to form more poleward in the warmer simulations (Figure 2b), these TCs have less time to grow in size before 40°, which would explain the larger probabilities of smaller storms in the warmer simulations compared to the cooler simulations. However, the TCs in the warmer simulations that do form closer to the equator grow larger in outer size than those in the cooler simulations and explain the longer extreme right tail. This, along with the increase in global mean TC outer size shown in Figure 3, suggests that there is a relationship between SST and outer size or SST and TC growth rate in these simulations. The flatter distributions with warmer SSTs may also be related to physical characteristics of the TCs themselves. Cronin and Chavas (2019) ran limited-domain rotating RCE simulations with various combinations of surface wetness and SST, and they found that TC outer size was more stable in time for TCs in the warm, moist environments. This suggests that in the warmer simulations, TCs that formed small tend to stay small and vice-versa, which would also explain the flatter outer size distributions at warmer SSTs.

We also explore the variability in another TC characteristic that impacts precipitation, TC intensity. Figure 5a shows the distributions of TC intensity. Only times when the TCs are equatorward of 40° are included; however, the increases in TC intensity with SST increases shown here are consistent at the global scale (not shown). The mean TC intensities (diamond markers on the *x*-axis) increase with increasing SST by about 1.5% per K. The maximum intensities that the TCs attain increase, as shown by the right tails extending further to the right. The 95th percentile TC intensity (circles on the top axis) increases with SST about 3.7% per K. Figure 5b shows the distributions of TC lifetime maximum intensities (LMIs). The mean LMI increases as the simulation SST

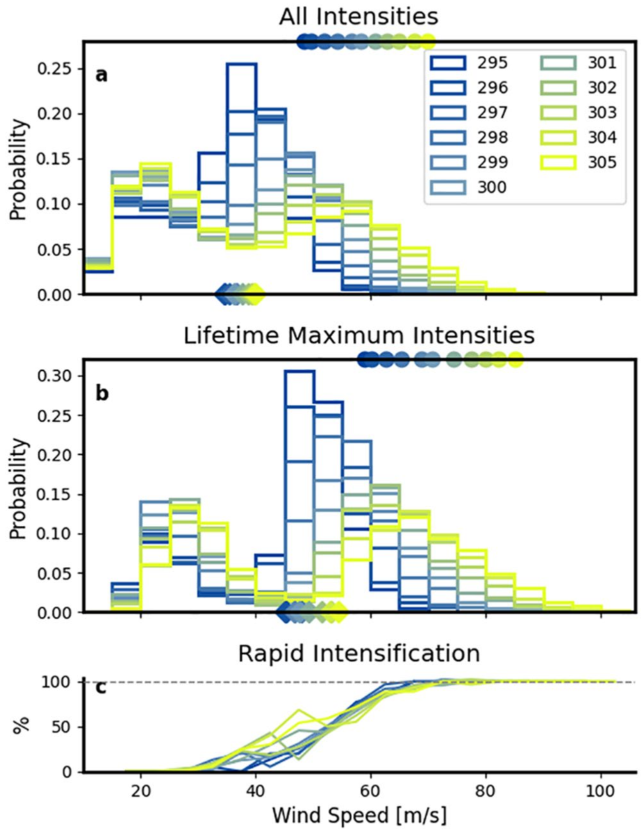

Figure 5. Distributions of (a) maximum wind speed (m s^{-1}) at all times in each tropical cyclone (TC) lifetime when the TC is equatorword of 40° and (b) lifetime maximum intensities (m s^{-1}) for all TCs that form equatorword of 40° for each model simulation. Maximum wind speeds are taken from the 2D TC low-level wind fields. The diamond markers on the *x*-axes indicate the mean of each distribution, and the circle markers on the top axes indicate the 95th percentile of each distribution. (c) The percentage of TCs in each 5 m s^{-1} bin that underwent rapid intensification at a time when they were equatorward of 40°.

gets warmer, consistent with Merlis et al. (2016). The maximum LMI also increases with warmer SST, as shown by the right tails of the distributions extending to higher wind speeds, which is consistent with TC PI theory. The 95th percentile values of LMI increase by 3.8% per K increase in SST, which is a faster rate than the increases in the means (1.4% per K) and over a larger range than the 95th percentiles of the distributions in Figure 5a.

All of the LMI distributions appear to be bimodal, with an initial peak around 30 m s^{-1} and a second peak ranging from around 50 m s^{-1} for the 295 K simulation to around 70 m s^{-1} for the 305 K simulation. These two peaks at least partially reflect differences in the latitudes of genesis. TCs with LMIs less than 40 m s^{-1} form on average 4.3° more poleward than TCs with LMIs greater than 40 m s^{-1}. This bimodal nature of LMI is also observed in the real world, and Lee et al. (2016) found that TC rapid intensification (RI) is an important cause of the bimodality since 79% of major TCs experience RI. RI is defined as a maximum wind speed increase of at least 30 kt (15.4 m s^{-1}) in 24 hr (definition from the National Hurricane Center). Only instances of RI that occur equatorward of 40° are counted. The percent of TCs that experience RI increases from 16.5% in the 295 K simulation to 42.6% in the 305 K simulation. Both observational (Kaplan & DeMaria, 2003) and theoretical (K. Emanuel, 2012) studies have shown that environments with higher PI, higher SST, and more mid-level moisture are favorable for RI. Since the warmer simulations have consistently higher PI (Figure S3 in Supporting Information S1) and greater mid-level moisture (Figure S4 in Supporting Information S1), the likelihood of RI is increased. Figure 5c shows the percentage of TCs in each 5 m s^{-1} intensity bin that underwent RI. This plot supports the assertion that the TCs that reach higher intensities undergo RI, especially for the warmer simulations, since the RI percentage is low for the lower intensity peak and much higher for majority of the secondary peaks in Figure 5b. One caveat is that for the model simulations, the wind at the lowest model level (around 60 m) is used to calculate instances of RI while for observations the 10 m wind speed is used; however, the authors do not expect this difference to impact the overall results. The increase of RI instances with warmer SSTs is consistent with recent studies showing a significant increase in the proportion of TCs that underwent RI in the Atlantic Basin between 1982 and 2009 (Bhatia et al., 2019) and projecting an increase in the likelihood of RI due to climate change using a high-resolution climate model (Bhatia et al., 2018).

3.2. TC Precipitation

3.2.1. Analysis of Precipitation Intensity, Field, and Structure

With the results from Section 3.1 in mind, we now analyze changes in TC precipitation with warming SST in these simulations in various ways. To provide some context on the contribution of TCs to the total precipitation in these RCE simulations, it was calculated that the mean percentage of total global precipitation that comes from TCs ranges between 41% and 51%. The rest of the precipitation comes from equatorial waves and other convective systems near the equator, but for this work, we focus on the TCs. Figure 6 shows spatial composites of 3-hourly averaged TC precipitation for TCs of all intensities, separated by model simulation. These composites show the general structure expected of a TC, including an eye in the center with relatively low precipitation rates and an area of the most intense precipitation surrounding the eye, with precipitation then decreasing moving outward from the center. Note, we don't expect a rain-free eye in these simulations as the precipitation variable is averaged over 3-hr intervals and the storms are moving over the average time period. Also, since these are composites of thousands of snapshots of precipitation throughout the TCs' lifetimes, we do not expect to see any small-scale structures, such as rainbands. The composites only include times when the TCs are equatorward of 40° to exclude TCs that form near the poles due to tracker specifications. The most striking change in these composites is the

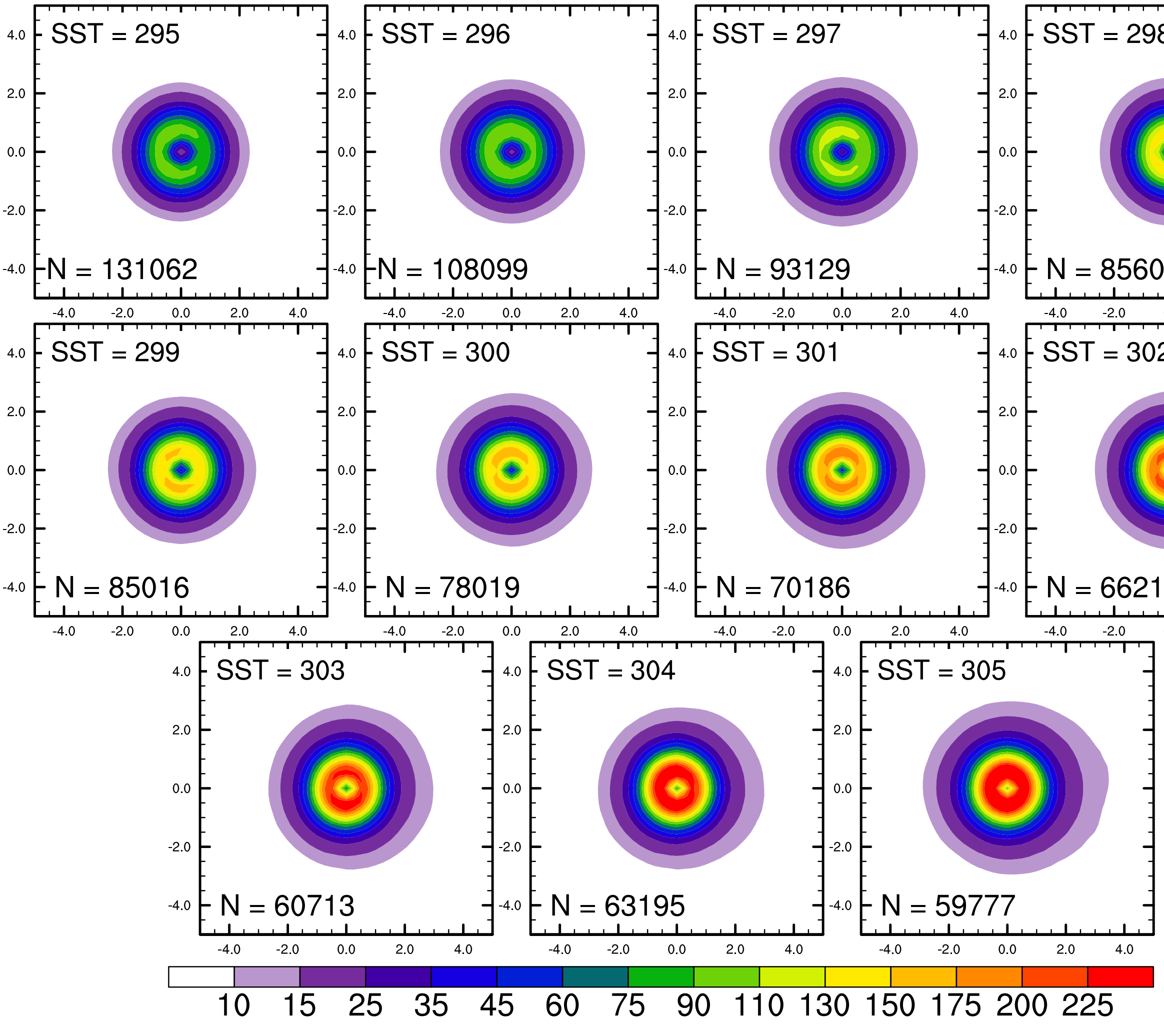

Figure 6. Composites of 3-hourly TC precipitation (mm day^{-1}) for each model simulation (SST listed in the top left of each panel). Only TCs equatorward of 40° are included. The number in the bottom left of each panel shows the number of samples that went into each composite. The units for both the *x* and *y* axes are great circle degrees.

increase in inner core precipitation as the simulation SST increases. There is also an increase in spatial extent of the precipitation field as the SST increases, which is most evident when comparing the 295 and 305 K simulation composites. To show another perspective, azimuthal-mean TC precipitation profiles were calculated for all TCs equatorward of 40° (Figure S5 in Supporting Information S1). These profiles show the monotonic increase in TC precipitation with increasing SST, especially in the inner cores of the storms.

To estimate the mean TC precipitation percentage change per degree of warming using these composites, 1,000 random TC precipitation snapshots are extracted from all of the available snapshots and averaged together to create a composite for each model simulation. The mean percentage change is calculated for each pair of simulations, using 295 and 296 K, 296 and 297 K, and so on. This process is repeated 10,000 times for each simulation pair, and then an overall mean and confidence intervals are calculated from the 100,000 samples, similar to the statistical method of bootstrapping. The mean TC precipitation increase calculated using this technique is 7.4% per K, with 95% confidence intervals of 1.63% and 13.84% per K. The means for each 10,000 sample simulation pair range between 4.8% and 11.1% per K. If instead of using all of the model simulations, only the temperatures used for RCEMIP (295, 300, and 305 K) are used in these calculations, the mean with 95% confidence intervals is 8.5% per K (7.10%–10.07% per K), calculated using the 20,000 samples. Both of the mean estimates are above the C-C scaling for precipitation increases with warming, but the mean estimate only using the official RCEMIP temperatures is greater than using all of the simulations.

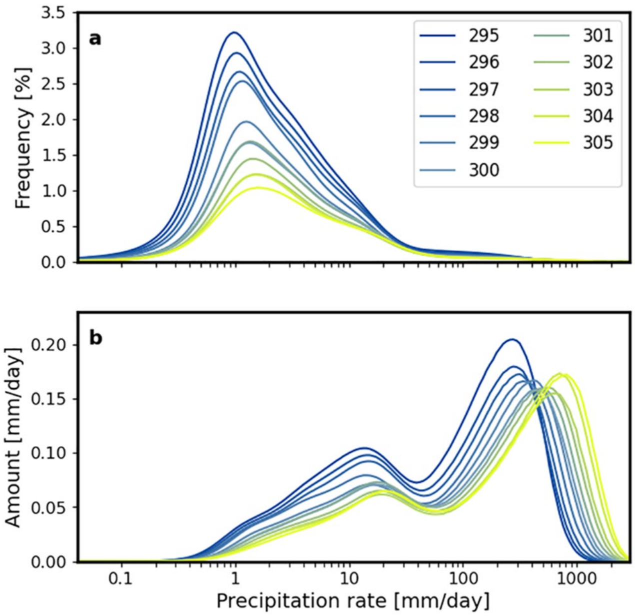

Figure 7. Distributions of TC precipitation rate (a) frequencies (%) and (b) amounts (mm day^{-1}) for each model simulation. The *x*-axis shows precipitation rates within TCs, binned on a logarithmic scale (see Section 2.3 for more details about the binning). The frequency represents the percentage of TC precipitation that comes from each precipitation rate bin, while the amount shows the total precipitation amount that comes from each precipitation rate bin. Only precipitation rates that occur equatorward of 40° are included.

Figure 7a shows the distributions of 3-hourly TC precipitation rate frequency for each model simulation. Again, only gridpoints equatorward of 40° are included in both distributions. The frequency on the *y*-axis represents the percentage of TC precipitation that comes from each precipitation rate on the *x*-axis. As the simulation SST increases, the frequency of most precipitation rates decreases while the extremely high precipitation rates in the extreme right tail increase. The decrease in frequency as SST increases across most of the distribution is likely due to the decrease in TC occurrences with increasing SST (Figure 2a). Figure 7b shows the distributions of TC precipitation amount in mm day^{-1} for each model simulation. The amount on the *y*-axis shows the total precipitation amount that comes from each precipitation rate on the *x*-axis. In all model simulations, the extreme precipitation rates (greater than 100 mm day^{-1}) contribute the largest TC precipitation amounts. As the SST increases, the most extreme precipitation rates grow, as shown by the right tails extending further to the right on the *x*-axis. Also the precipitation rate that contributes the greatest precipitation amount gets larger as SST increases. For precipitation rates to the left of the distributions peaks, the warmer simulations tend to show lower precipitation amounts, which could be due to the decreased TC occurrences or could indicate that less TC precipitation comes from lighter precipitation rates.

3.2.2. Dependence of Precipitation on SST, TC Intensity, and TC Outer Size

In an attempt to disentangle how much of the TC precipitation increases shown in Figures 6 and 7 come from changes in TC intensity and outer size (discussed in Section 3.1.2), joint dependence plots for TC precipitation are created (Figure 8).

These plots show how 99th percentile (a and c) and accumulated (b and d) TC precipitation vary with SST and TC intensity changes (a and b) and with SST and TC outer size changes (c and d). The 99th percentile precipitation represents the value above which only 1% of precipitation occurs for each TC at each 3-hourly snapshot in its lifetime, while accumulated precipitation is the sum of all precipitation for each TC at each 3-hourly snapshot in its lifetime. The accumulated TC precipitation, as defined here, is a spatial accumulation. These values are calculated using the TC precipitation regridded onto a cartesian grid with 0.25° grid spacing using TempestExtremes (Ullrich et al., 2021), which is the same grid used to create the composites in Figure 6. While, regridding does impact the precipitation statistics, the plots in Figure 8 are very similar to those created using the precipitation on the native model grid (Figure S6 in Supporting Information S1).

Each colored box shows the median value of the distribution of the given TC precipitation metric for all TCs at every SST and intensity or SST and outer size combination. For example, the box all the way to the top left in Figure 8a shows the median 99th percentile precipitation value calculated using all TCs in the 305 K simulation that have intensities between 20 and 25 m s^{-1}. The pink line contours show the number of samples in each box, and only boxes with sample sizes over 100 are plotted. The line plots below each joint dependence plot show the mean percentage change in precipitation per change in K for each intensity or size bin. It is calculated by taking the mean of the percentage change in precipitation calculated using every pair of boxes (representing a change of 1 K) along each vertical column. The line plots to the left of the joint dependence plots show the percentage change in precipitation per change in intensity (a and b) or outer size (c and d) for each simulation SST. It is calculated by taking the mean of the percentage change in precipitation calculated using every pair of boxes along each horizontal row.

Starting with Figures 8a and 8b, the SST and TC intensity joint dependence plots, we see that both TC precipitation metrics increase as SST and TC intensity increase, demonstrated by the maximum in the top right corner of each plot. The boxes with no color in the bottom right show how the cooler simulations do not have the very intense TCs that the warmer simulations do, consistent with Figure 5. Looking at the line plots to the left of the joint dependence plots, Figure 8a has a percentage increase in precipitation per intensity change between 2.5%

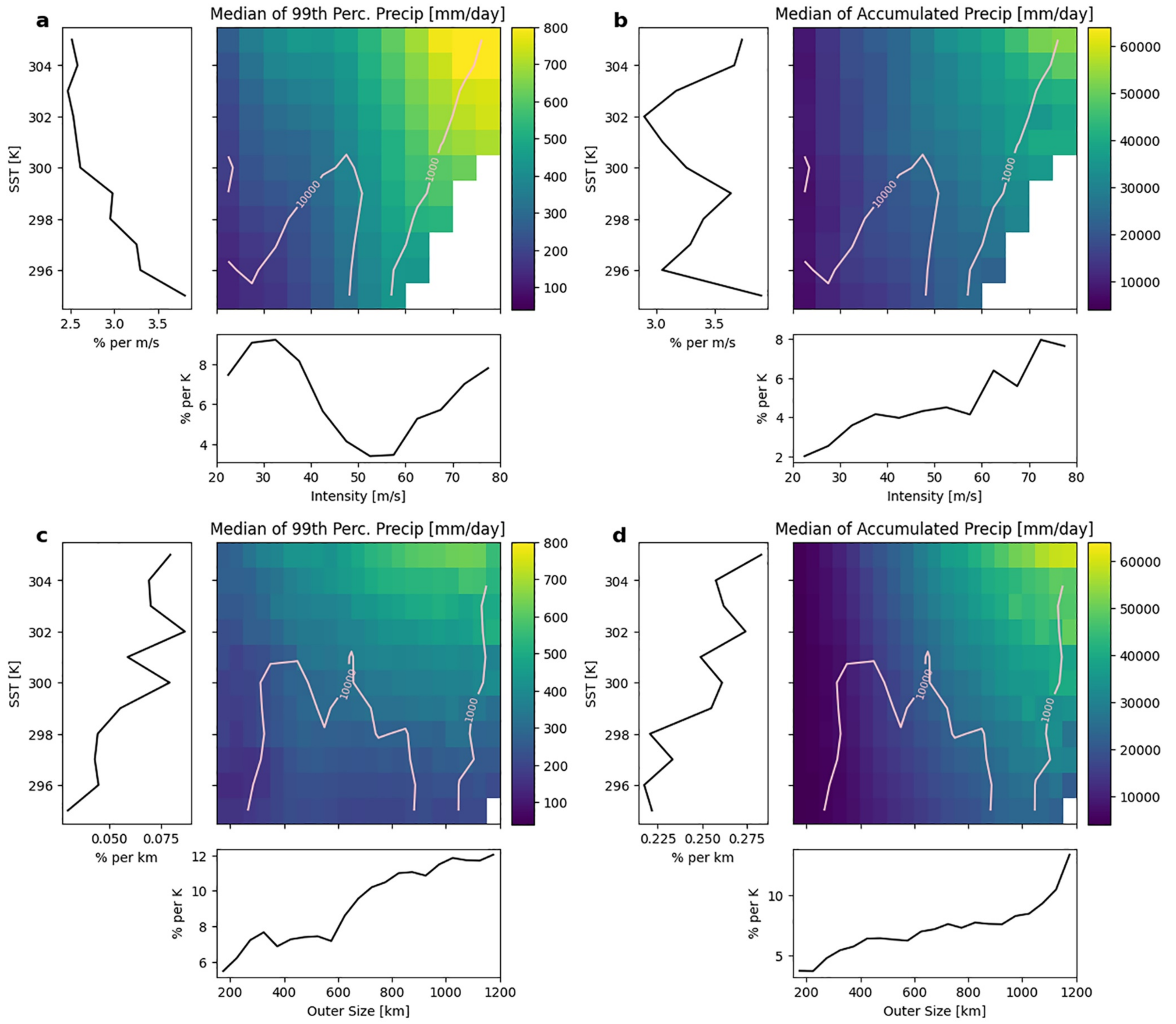

Figure 8. Dependence of TC precipitation (mm day^{-1}) on (a), (b) TC intensity (m s^{-1}) and simulation SST (K) and (c), (d) TC size (km) and simulation SST (K). The precipitation variables are (a), (c) 99th percentile TC precipitation and (b), (d) accumulated TC precipitation. For a and b, the data are binned into 5 m s^{-1} bins on the intensity axis and 1 K bins on the SST axis, while for c and d, the data are binned into 50 km bins on the size axis and 1 K bins on the SST axis. The median value of each precipitation variable is displayed in each bin (color). The pink contours denote bin counts for $N = (1000, 10{,}000)$, and only bins with greater than 100 samples are shown. The line plots to the left of each joint dependence plot show the percentage change in precipitation per change in (a), (b) TC intensity or (c), (d) TC size, which is calculated by averaging the percentage change between each bin over each horizontal row. The line plots below each joint dependence plot show the percentage change in precipitation per change in SST, which is calculated by averaging the percentage change between each bin over each vertical column.

and 3.8% per m s^{-1} while the values for the accumulated precipitation in Figure 8b are between 3.0% and 4.0% per m s^{-1}. The line in Figure 8a has a decreasing trend as SST increases, suggesting that the 99th percentile precipitation is less impacted by TC intensity as SST increases. The bottom line plot in Figure 8a shows that the percentage change in precipitation per SST change varies between 3.2% and 9.6% per K. The higher values occur in the 20–35 m s^{-1} TC intensity range, and then the values drop to their minimum around 55 m s^{-1} but increase again at the higher TC intensities. On the other hand, the percentage change in precipitation per SST change in Figure 8b almost consistently increases across the TC intensity range from 2.0% to 7.9% per K. These bottom plots show that estimates of percentage change in precipitation per SST change can be influenced by the specific precipitation variable, TC intensities, and potentially the bin sizes, but the order of magnitude is consistent.

Moving on to Figures 8c and 8d, the SST and TC outer size joint dependence plots, we see different patterns between the 99th percentile and accumulated TC precipitation. While the 99th percentile precipitation does increase with SST warming, it does not change as much with outer size increases. On the other hand, the accumulated precipitation again has a maximum in the upper right corner, indicating that it increases with both SST and outer size. This makes sense, since as TCs get larger, there is likely a larger precipitation field, as shown in Figure 6. Figure 8c suggests that TC outer size changes have little impact on TC extreme precipitation, especially in the lower end of the SST range. This is backed up by the line plot to the left, as the percentage change in precipitation per change in TC size is below 0.08% per km for all simulation SSTs. Looking at the left line plot in Figure 8d, the numbers are also small, less than 0.28% per km, with an increasing trend as simulation SST increases. For the bottom line plot in Figure 8c, the values of percentage change in precipitation per SST change vary between 5.5% and 12.0% per K and for the most part increase as TC outer size increases. The values in Figure 8d are similar, varying between 3.7% and 13.4% per K, and also show an increasing trend as TC outer size increases. These bottom line plots are similar for both 99th percentile and accumulated TC precipitation, and the magnitudes of change are comparable to those in Figures 8a and 8b.

3.2.3. Estimating Thermodynamic and Dynamic Contributions to TC Precipitation Change

While Figure 8 shows that TC precipitation depends on both TC intensity and outer size changes, it is still unclear how much these dynamic changes control precipitation changes compared to environmental thermodynamic changes in the simulations. Higher SSTs should fuel higher evaporation rates, which increase the amount of precipitable water in the atmosphere and therefore lead to greater precipitation rates. To break down the contributions to TC precipitation increases into partial changes from SST, TC intensity (V), and TC outer size (R), an equation is developed based on partial derivatives:

$$\frac{dP(SST, V, R)}{dSST} \approx \frac{\partial_{V,R}P}{\partial SST} + \frac{\partial_{SST,R}P}{\partial V}\frac{\partial V}{\partial SST} + \frac{\partial_{SST,V}P}{\partial R}\frac{\partial R}{\partial SST} \tag{1}$$

On the left hand side, $\frac{dP(SST,V,R)}{dSST}$ is the total percentage change in TC precipitation per SST change in units of % per K, and its value is estimated from the percentage change of the means of the distributions of 99th percentile and accumulated TC precipitation including all TC snapshots equatorward of 40°. The first term on the right hand side represents the thermodynamic contribution to TC precipitation change, meaning the percentage change in TC precipitation due to just SST assuming intensity and outer size remain constant. The second and third terms on the right hand side represent the dynamic contributions to TC precipitation change from TC intensity and outer size change, respectively.

$\frac{\partial V}{\partial SST}$ and $\frac{\partial R}{\partial SST}$ are estimated from ordinary linear regression using the mean TC intensities and outer sizes (discussed in Section 3.1.2) calculated using all TCs equatorward of 40°. Note that we also calculated $\frac{\partial V}{\partial SST}$ and $\frac{\partial R}{\partial SST}$ using ordinary linear regression with all of the intensity and outer size values equatorward of 40°, instead of just the means, and got the same answer for $\frac{\partial V}{\partial SST}$ and a very similar value for $\frac{\partial R}{\partial SST}$. While the $\frac{\partial V}{\partial SST}$ value is smaller than calculated for PI using a single-column model (Ramsay & Sobel, 2011), the sensitivity of PI to SST $\left(\frac{\partial PI}{\partial SST}\right)$ calculated for 40°S–40°N for our simulations is 1.6 m s^{-1} per K, which is similar to the value of 1.4 m s^{-1} per K from Ramsay and Sobel (2011). $\frac{\partial_{V,R}P}{\partial SST}$, $\frac{\partial_{SST,R}P}{\partial V}$, and $\frac{\partial_{SST,V}P}{\partial R}$ are estimated using a Poisson (log link) regression, a generalized linear model form of regression analysis:

$$P = c * e^{b_1 * SST + b_2 * V + b_3 * R} \tag{2}$$

The values of SST, V, and R, the independent variables, and P, the dependent variable, for all TCs at all times when they are equatorward of 40° are incorporated into the regression. P is estimated from the individual TC precipitation snapshots that went into the precipitation composites in Figure 6, while V and R are taken from the output of the TempestExtremes TC tracker at the time of each snapshot. To clarify, V is the TC's maximum wind speed at the lowest model level, and R is the radius of the 8 m s^{-1} wind speed, calculated from the azimuthally averaged azimuthal wind speeds at the lowest model level. From this Poisson regression, the estimate of the percentage contribution to TC precipitation change from SST, V, and R, independent of the influence from the other two variables, can be estimated from the regression coefficients. For example, $\frac{\partial_{V,R}P}{\partial SST}$ is calculated as $(e^{b_1} - 1) * 100\%$. Poisson regression is chosen because all of the TC precipitation values are greater than 0, and the exponential scaling aligns with Clausius-Clapeyron scaling. Equations 1 and 2 are calculated twice, once using the 99th percentile TC precipitation as P and once using the accumulated TC precipitation as P. All of the estimates for the terms in Equation 1 are reported in Table 1.

Table 1

Values for Terms in Equation 1. The Percentages in Parenthesis Next to Certain Values Represent That Term's Percentage Contribution to the Total TC Precipitation Change ($\frac{dP(SST,V,R)}{dSST}$*). These Percentages Will Not Add up to 100% Because There Are Residuals*

	99th percentile	Accumulated
Calculated from Distribution Means		
$\frac{dP(SST,V,R)}{dSST}$ (% per K)	8.6	6.6
Calculated using Linear Regression		
$\frac{\partial V}{\partial SST}$ (m s^{-1} per K)	0.6	–
$\frac{\partial R}{\partial SST}$ (km per K)	−2.8	–
Calculated using Poisson Regression		
$\frac{\partial_{V,R}P}{\partial SST}$ (% per K)	5.8 (67%)	5.1 (77%)
$\frac{\partial_{SST,R}P}{\partial V}$ (% per m s^{-1})	2.9	1.3
$\frac{\partial_{SST,R}P}{\partial V} * \frac{\partial V}{\partial SST}$ (% per K)	1.7 (20%)	0.8 (12%)
$\frac{\partial_{SST,V}P}{\partial R}$ (% per km)	−0.1	0.2
$\frac{\partial_{SST,V}P}{\partial R} * \frac{\partial R}{\partial SST}$ (% per K)	0.3 (3%)	−0.6 (−9%)

First for 99th percentile precipitation, $\frac{dP(SST,V,R)}{dSST}$ is estimated to be 8.6% per K with 95th percentile confidence intervals of 3.61% and 12.78% per K, calculated using bootstrap analysis. Note that this estimate of percentage change in TC precipitation per K of warming, using the 99th percentile TC precipitation, is different than the estimate in Section 3.2.1 calculated for the mean TC precipitation. All of the terms on the right hand side of Equation 1 add up to 7.8% per K, leaving a residual of 0.8% per K. This residual could be related to other factors that influence TC precipitation, such as changes in vertical stability or microphysical changes. TC intensity changes contribute about 20% (i.e., $\frac{1.7}{8.6} * 100\%$) to 99th percentile precipitation increases, while thermodynamic changes contribute about 67%. Outer size changes have the smallest effect, decreasing TC 99th percentile precipitation by about 0.3% per K. For accumulated TC precipitation, $\frac{dP(SST,V,R)}{dSST}$ is estimated at 6.6% per K, less than the value for 99th percentile precipitation, with 95th percentile confidence intervals of 2.53% and 11.58% per K. The sum of the right hand terms of Equation 1 is 5.3% per K, resulting in a 1.3% per K residual. Besides the factors mentioned for 99th percentile precipitation, the translation speeds of the TCs may contribute to the residual for accumulated precipitation. The contribution from TC intensity increase is about 12% of the total, and the thermodynamic contribution is about 77%, again demonstrating that changes in both SST and storm intensity play an important role in TC precipitation changes. Outer size changes contribute about −9% to accumulated precipitation changes, a larger influence than for 99th percentile precipitation. The outer size contribution calculated for accumulated precipitation is negative because the change in outer size per change in SST $\left(\frac{\partial R}{\partial SST}\right)$ is negative for TCs equatorward of 40°. It is clear from this analysis that the outer size changes contribute more to the change in accumulated precipitation than 99th percentile precipitation change, while SST and intensity changes contribute significantly to both precipitation metrics. Additionally, estimates of TC precipitation percentage changes due to warming are dependent on the precipitation metric chosen. Note, Equations 1 and 2 were recalculated using the TC central pressure deficit (background sea level pressure minus the TCs' minimum sea level pressures), following Chavas et al. (2017), as the measure of TC intensity instead of the maximum wind speeds. Using this different measure of intensity didn't greatly impact the results and the overall conclusions remained the same. See Figure S7 in the Supporting Information S1 for plots similar to Figures 8a and 8b, except using central pressure deficit as the measure of TC intensity.

4. Conclusions

To quantify how TC precipitation is impacted by warming, idealized global CAM rotating RCE simulations were run using globally uniform SSTs ranging between 295 and 305 K. Protocols of RCEMIP (Wing et al., 2018) were followed, except the simulations included planetary rotation. These conditions result in "TC worlds," where TCs form in the lower latitudes, move westward and poleward, and accumulate near the poles. As the simulation SST increases, the average number of TCs decreases, while the TCs tend to have larger outer sizes. The percentage of the globe covered by TCs also decreases, showing that the TC count decrease outpaces the outer size increase. The latitudes of maximum genesis move slightly poleward with surface warming, and the TCs tend to reach higher intensities with more storms undergoing rapid intensification. These results are generally consistent with those seen in similar "TC world" global simulations, such as Merlis et al. (2016), Chavas and Reed (2019), and Walsh et al. (2020). For the analysis of TC precipitation, only TCs within 40°S and 40°N are included. This is to limit the analysis to areas where TC behavior is similar to real-world TCs, since closer to the poles in these simulations, TCs frequently interact. While between 40°S and 40°N, the spatial coverage of TCs still decreases as SST increases, the mean outer sizes are similar for all the simulations.

The highest precipitation rates within TCs become more extreme with surface warming. Additionally, very extreme precipitation rates within the TCs become more likely in the warmer SST simulations. For all simulations, large fractions of the TC precipitation amounts come from these extreme rates. The response of TC precipitation to intensity and outer size changes varies depending on whether its a metric of extreme precipitation or not. Both extreme (99th percentile) and accumulated TC precipitation increase with SST and intensity increases; however, accumulated precipitation seems to be more impacted by TC outer size changes than 99th percentile precipitation. TC precipitation rate increases with intensity increase is in agreement with previous research using both models (Moon et al., 2020; Vannière et al., 2020) and observations (Lavender & McBride, 2021; Rios Gaona et al., 2018). While limited work has been done looking at the relationship between TC size and precipitation, Lavender and McBride (2021) found higher radially averaged precipitation rates in TCs with greater radii of 34 kt winds using the TRMM 3B42 data set.

The overall change in TC precipitation per change in SST was estimated to be 8.6% per K for 99th percentile precipitation and 6.6% per K for accumulated precipitation. While the accumulated precipitation increase is right around the C-C rate, the 99th percentile increase is greater than the C-C rate. Using Equation 1 to break down the precipitation increases into partial components, TC intensity was estimated to contribute about 20% for 99th percentile precipitation changes and 12% for accumulated precipitation changes. While, TC outer size contributed a 3% increase to 99th percentile precipitation changes, it was estimated to contribute a 9% decrease for accumulated precipitation changes. The decrease comes from the fact that mean TC outer sizes decreased with increasing SST equatorward of 40°. The thermodynamic contribution to TC precipitation increases was estimated to be 67% for 99th percentile and 77% for accumulated TC precipitation. These results support the conclusion that thermodynamic changes (e.g., SST) cause a majority of the TC precipitation increases, while TC intensity contributes secondarily to the TC precipitation increase in these simulations. TC outer size only substantially impacts measures of accumulated precipitation.

How do these changes in TC precipitation in these simplified model simulations relate to TCs in the real world? Application of this TC precipitation analysis framework, especially the joint dependence plots in Figure 8, to more realistic model simulations and observations will help answer this question in future work. One strength of this framework is a consistent methodology applied across models and observations, including using TempestExtremes to track TCs, extract TC precipitation, and composite TC precipitation. As shown in Chavas et al. (2017), TC structure was similar between global RCE simulations, more realistic Earth-like model simulations, and observations, which suggests comparing TC precipitation might provide similar results. Another advantage is that RCE simulations are relatively short and computationally inexpensive, but they provide a large number of TC samples for estimating precipitation changes. These simulations produce hundreds of TCs per year, while in the real world, there are only around 90 TCs globally per year. This allows us to develop estimates of TC precipitation increases using the tens of thousands of TC snapshots and then explore how these estimates compare to Earth-like simulations and observations.

Data Availability Statement

The model data used for this study are available on the Dryad Digital Repository via https://doi.org/10.506\,1/dryad.x3ffbg7jv (Stansfield & Reed, 2021). Computing and data storage resources, including the Cheyenne supercomputer (doi:10.5065/D6RX99HX), were provided by the Computational and Information Systems Laboratory (CISL) at NCAR. NCAR is sponsored by the National Science Foundation.

Acknowledgments
The authors thank Daniel Chavas and Levi Silvers for their feedback and suggestions that substantially improved the manuscript. Stansfield and Reed acknowledge the support the Department of Energy Office of Science award number DE-SC0016605, "A Framework for Improving Analysis and Modeling of Earth System and Intersectoral Dynamics at Regional Scales." Reed also recognizes partial support from the National Science Foundation (Grant AGS-1830729). Stansfield also recognizes support from the National Science Foundation (Grant DGE-1633299).

References

Bacmeister, J. T., Reed, K. A., Hannay, C., Lawrence, P., Bates, S., Truesdale, J. E., et al. (2018). Projected changes in tropical cyclone activity under future warming scenarios using a high-resolution climate model. *Climatic Change*, *146*(3–4), 547–560. https://doi.org/10.1007/s10584-016-1750-x

Banzon, V., Smith, T. M., Chin, T. M., Liu, C. Y., & Hankins, W. (2016). A long-term record of blended satellite and in situ sea-surface temperature for climate monitoring, modeling and environmental studies. *Earth System Science Data*, *8*, 165–176. https://doi.org/10.5194/essd-8-165-2016

Bhatia, K. T., Vecchi, G. A., Knutson, T. R., Murakami, H., Kossin, J., Dixon, K. W., & Whitlock, C. E. (2019). Recent increases in tropical cyclone intensification rates. *Nature Communications*, *10*(1), 1–9. https://doi.org/10.1038/s41467-019-08471-z

Bhatia, K. T., Vecchi, G. A., Murakami, H., Underwood, S., & Kossin, J. (2018). Projected response of tropical cyclone intensity and intensification in a global climate model. *Journal of Climate*, *31*(20), 8281–8303. https://doi.org/10.1175/JCLI-D-17-0898.1

Bony, S., Stevens, B., Coppin, D., Becker, T., Reed, K. A., Voigt, A., & Medeiros, B. (2016). Thermodynamic control of anvil cloud amount. *Proceedings of the National Academy of Sciences*, *113*(32), 8927–8932. https://doi.org/10.1073/pnas.1601472113

Bretherton, C. S., Blossey, P. N., & Khairoutdinov, M. (2005). An energy-balance analysis of deep convective self-aggregation above uniform SST. *Journal of the Atmospheric Sciences*, *62*(12), 4273–4292. https://doi.org/10.1175/JAS3614.1

Carstens, J. D., & Wing, A. A. (2020). Tropical cyclogenesis from self-aggregated convection in numerical simulations of rotating radiative-convective equilibrium. *Journal of Advances in Modeling Earth Systems*, *12*(5), e2019MS002020. https://doi.org/10.1029/2019MS002020

Chan, J. C. (2005). The physics of tropical cyclone motion. *Annual Review of Fluid Mechanics*, *37*(1), 99–128. https://doi.org/10.1146/annurev.fluid.37.061903.175702

Chavas, D. R., & Emanuel, K. A. (2014). Equilibrium tropical cyclone size in an idealized state of axisymmetric radiative–convective equilibrium. *Journal of the Atmospheric Sciences*, *71*(5), 1663–1680. https://doi.org/10.1175/JAS-D-13-0155.1

Chavas, D. R., Lin, N., Dong, W., & Lin, Y. (2016). Observed tropical cyclone size revisited. *Journal of Climate*, *29*(8), 2923–2939. https://doi.org/10.1175/JCLI-D-15-0731.1

Chavas, D. R., & Reed, K. A. (2019). Dynamical aquaplanet experiments with uniform thermal forcing: System dynamics and implications for tropical cyclone genesis and size. *Journal of the Atmospheric Sciences*, *76*, 2257–2274. https://doi.org/10.1175/JAS-D-19-0001.1

Chavas, D. R., Reed, K. A., & Knaff, J. A. (2017). Physical understanding of the tropical cyclone wind-pressure relationship. *Nature Communications*, *8*(1), 1360. https://doi.org/10.1038/s41467-017-01546-9

Cronin, T. W., & Chavas, D. R. (2019). Dry and semidry tropical cyclones. *Journal of the Atmospheric Sciences*, *76*(8), 2193–20. https://doi.org/10.1175/JAS-D-18-0357.1

Cronin, T. W., & Wing, A. A. (2017). Clouds, circulation, and climate sensitivity in a radiative-convective equilibrium channel model. *Journal of Advances in Modeling Earth Systems*, *9*(8), 2883–2905. https://doi.org/10.1002/2017MS001111

Danabasoglu, G., Lamarque, J.-F., Bacmeister, J., Bailey, D., DuVivier, A., Edwards, J., et al. (2020). The community earth system model version 2 (CESM2). *Journal of Advances in Modeling Earth Systems*, *12*(2), e2019MS001916. https://doi.org/10.1029/2019MS001916

Dennis, J. M., Edwards, J., Evans, K. J., Guba, O., Lauritzen, P. H., Mirin, A. A., et al. (2012). CAM-SE: A scalable spectral element dynamical core for the Community Atmosphere Model. *International Journal of High Performance Computing Applications*, *26*(1), 74–89. https://doi.org/10.1177/1094342011428142

Emanuel, K. (2012). Self-stratification of tropical cyclone outflow. Part II: Implications for storm intensification. *Journal of the Atmospheric Sciences*, *69*(3), 988–996. https://doi.org/10.1175/JAS-D-11-0177.1

Emanuel, K. A. (1999). Thermodynamic control of hurricane intensity. *Nature*, *401*(6754), 665–669. https://doi.org/10.1038/44326

Emanuel, K. A. (2017). Assessing the present and future probability of Hurricane Harvey's rainfall. *Proceedings of the National Academy of Sciences*, *114*(48), 12681–12684. https://doi.org/10.1073/pnas.1716222114

Eyring, V., Bony, S., Meehl, G. A., Senior, C. A., Stevens, B., Stouffer, R. J., & Taylor, K. E. (2016). Overview of the Coupled Model Intercomparison Project Phase 6 (CMIP6) experimental design and organization. *Geoscientific Model Development*, *9*(5), 1937–1958. https://doi.org/10.5194/gmd-9-1937-2016

Gutmann, E. D., Rasmussen, R. M., Liu, C., Ikeda, K., Bruyere, C. L., Done, J. M., et al. (2018). Changes in hurricanes from a 13-yr convection-permitting pseudo–global warming simulation. *Journal of Climate*, *31*(9), 3643–3657. https://doi.org/10.1175/JCLI-D-17-0391.1

Guzman, O., & Jiang, H. (2021). Global increase in tropical cyclone rain rate. *Nature Communications*, *12*. https://doi.org/10.1038/s41467-021-25685-2

Held, I. M., & Zhao, M. (2008). Horizontally homogeneous rotating radiative–convective equilibria at GCM resolution. *Journal of the Atmospheric Sciences*, *65*(6), 2003–2013. https://doi.org/10.1175/2007jas2604.1

Hsieh, T.-L., Vecchi, G. A., Yang, W., Held, I. M., & Garner, S. T. (2020). Large-scale control on the frequency of tropical cyclones and seeds: A consistent relationship across a hierarchy of global atmospheric models. *Climate Dynamics*, *55*(11), 3177–3196. https://doi.org/10.1007/s00382-020-05446-5

Kaplan, J., & DeMaria, M. (2003). Large-scale characteristics of rapidly intensifying tropical cyclones in the North Atlantic basin. *Weather and forecasting*, *18*(6), 10932–1108. https://doi.org/10.1175/1520-0434(2003)018<1093:lcorit>2.0.co;2

Kim, H.-S., Vecchi, G. A., Knutson, T. R., Anderson, W. G., Delworth, T. L., Rosati, A., et al. (2014). Tropical cyclone simulation and response to CO_2 doubling in the GFDL CM2. 5 high-resolution coupled climate model. *Journal of Climate*, *27*(21), 8034–8054. https://doi.org/10.1175/JCLI-D-13-00475.1

Knapp, K. R., Kruk, M. C., Levinson, D. H., Diamond, H. J., & Neumann, C. J. (2010). The international best track archive for climate stewardship (IBTrACS) unifying tropical cyclone data. *Bulletin of the American Meteorological Society*, *91*(3), 363–376. https://doi.org/10.1175/2009BAMS2755.1

Knutson, T. R., Camargo, S. J., Chan, J. C., Emanuel, K. A., Ho, C.-H., Kossin, J., et al. (2020). othersTropical cyclones and climate change assessment: Part II. Projected response to anthropogenic warming. *Bulletin of the American Meteorological Society*, *101*(3), E303–E322. https://doi.org/10.1175/BAMS-D-18-0194.1

Knutson, T. R., Sirutis, J. J., Vecchi, G. A., Garner, S., Zhao, M., Kim, H.-S., et al. (2013). Dynamical downscaling projections of twenty-first-century atlantic hurricane activity: Cmip3 and cmip5 model-based scenarios. *Journal of Climate*, *26*(17), 6591–6617. https://doi.org/10.1175/JCLI-D-12-00539.1

Knutson, T. R., Sirutis, J. J., Zhao, M., Tuleya, R. E., Bender, M., Vecchi, G. A., et al. (2015). Global projections of intense tropical cyclone activity for the late twenty-first century from dynamical downscaling of CMIP5/RCP4. 5 scenarios. *Journal of Climate*, *28*(18), 7203–7224. https://doi.org/10.1175/JCLI-D-15-0129.1

Knutson, T. R., & Tuleya, R. E. (2004). Impact of co2-induced warming on simulated hurricane intensity and precipitation: Sensitivity to the choice of climate model and convective parameterization. *Journal of Climate*, *17*(18), 3477–3495. https://doi.org/10.1175/1520-0442(2004)017<3477:iocwos>2.0.co;2

Lauritzen, P. H., Nair, R. D., Herrington, A. R., Callaghan, P., Goldhaber, S., Dennis, J. M., et al. (2018). NCAR release of CAM-SE in CESM2. 0: A reformulation of the spectral element dynamical core in dry-mass vertical coordinates with comprehensive treatment of condensates and energy. *Journal of Advances in Modeling Earth Systems*, *10*(7), 1537–1570. https://doi.org/10.1029/2017MS001257

Lavender, S. L., & McBride, J. L. (2021). Global climatology of rainfall rates and lifetime accumulated rainfall in tropical cyclones: Influence of cyclone basin, cyclone intensity and cyclone size. *International Journal of Climatology*, *41*, E1217–E1235. https://doi.org/10.1002/joc.6763

Lee, C.-Y., Tippett, M. K., Sobel, A. H., & Camargo, S. J. (2016). Rapid intensification and the bimodal distribution of tropical cyclone intensity. *Nature Communications*, *7*(1), 1–5. https://doi.org/10.1038/ncomms1062510.1038/ncomms10625

Lin, Y., Zhao, M., & Zhang, M. (2015). Tropical cyclone rainfall area controlled by relative sea surface temperature. *Nature Communications*, *6*(1), 1–7. https://doi.org/10.1038/ncomms7591

Liu, M., Vecchi, G. A., Smith, J. A., & Knutson, T. R. (2019). Causes of large projected increases in hurricane precipitation rates with global warming. *npj Climate and Atmospheric Science*, *2*(1), 1–5. https://doi.org/10.1038/s41612-019-0095-3

Liu, M., Vecchi, G. A., Smith, J. A., & Murakami, H. (2018). Projection of landfalling–tropical cyclone rainfall in the Eastern United States under anthropogenic warming. *Journal of Climate*, *31*(18), 7269–7286. https://doi.org/10.1175/JCLI-D-17-0747.1

Merlis, T. M., & Held, I. M. (2019). Aquaplanet simulations of tropical cyclones. *Current Climate Change Reports*, *5*(3), 185–195. https://doi.org/10.1007/s40641-019-00133-y

Merlis, T. M., Zhou, W., Held, I. M., & Zhao, M. (2016). Surface temperature dependence of tropical cyclone-permitting simulations in a spherical model with uniform thermal forcing. *Geophysical Research Letters*, *43*(6), 2859–2865. https://doi.org/10.1002/2016GL067730

Moon, Y., Kim, D., Camargo, S. J., Wing, A. A., Sobel, A. H., Murakami, H., et al. (2020). Azimuthally averaged wind and thermodynamic structures of tropical cyclones in global climate models and their sensitivity to horizontal resolution. *Journal of Climate*, *33*(4), 1575–1595. https://doi.org/10.1175/JCLI-D-19-0172.1

Muller, C. J. (2013). Impact of convective organization on the response of tropical precipitation extremes to warming. *Journal of Climate*, *26*(14), 5028–5043. https://doi.org/10.1175/JCLI-D-12-00655.1

Muller, C. J., O'Gorman, P. A., & Back, L. E. (2011). Intensification of precipitation extremes with warming in a cloud-resolving model. *Journal of Climate*, *24*(11), 2784–2800. https://doi.org/10.1175/2011JCLI3876.1

Neale, R., Chen, C.-C., Gettelman, A., Lauritzen, P. H., Park, S., Williamson, D. L., et al. (2012). *Description of the NCAR community atmosphere model (CAM5.0) (NCAR tech. Note nos. NCAR/TN-486+STR)*. National Center for Atmospheric Research.

Nolan, D. S., Rappin, E. D., & Emanuel, K. A. (2007). Tropical cyclogenesis sensitivity to environmental parameters in radiative–convective equilibrium. *Quarterly Journal of the Royal Meteorological Society: A journal of the atmospheric sciences, applied meteorology and physical oceanography*, *133*(629), 2085–2107. https://doi.org/10.1002/qj.170

Patricola, C. M., & Wehner, M. F. (2018). Anthropogenic influences on major tropical cyclone events. *Nature*, *563*(7731), 339–346. https://doi.org/10.1038/s41586-018-0673-2

Pendergrass, A. G., & Hartmann, D. L. (2014). Two modes of change of the distribution of rain. *Journal of Climate*, *27*(22), 8357–8371. https://doi.org/10.1175/JCLI-D-14-00182.1

Pendergrass, A. G., Reed, K. A., & Medeiros, B. (2016). The link between extreme precipitation and convective organization in a warming climate: Global radiative-convective equilibrium simulations. *Geophysical Research Letters*, *43*(21), 11–445. https://doi.org/10.1002/2016GL071285

Popke, D., Stevens, B., & Voigt, A. (2013). Climate and climate change in a radiative-convective equilibrium version of ECHAM6. *Journal of Advances in Modeling Earth Systems*, *5*(1), 1–14. https://doi.org/10.1029/2012MS000191

Ramsay, H. A., Singh, M. S., & Chavas, D. R. (2020). Response of tropical cyclone formation and intensification rates to climate warming in idealized simulations. *Journal of Advances in Modeling Earth Systems*, *12*(10), e2020MS002086. https://doi.org/10.1029/2020MS002086

Ramsay, H. A., & Sobel, A. H. (2011). Effects of relative and absolute sea surface temperature on tropical cyclone potential intensity using a single-column model. *Journal of Climate*, *24*(1), 183–193. https://doi.org/10.1175/2010JCLI3690.1

Reed, K. A., Bacmeister, J. T., Rosenbloom, N. A., Wehner, M. F., Bates, S. C., Lauritzen, P. H., et al. (2015). Impact of the dynamical core on the direct simulation of tropical cyclones in a high-resolution global model. *Geophysical Research Letters*, *42*(9), 3603–3608. https://doi.org/10.1002/2015GL063974

Reed, K. A., & Chavas, D. R. (2015). Uniformly rotating global radiative-convective equilibrium in the Community Atmosphere Model, version 5. *Journal of Advances in Modeling Earth Systems*, *7*(4), 1938–1955. https://doi.org/10.1002/2015MS000519

Reed, K. A., & Jablonowski, C. (2012). Idealized tropical cyclone simulations of intermediate complexity: A test case for AGCMs. *Journal of Advances in Modeling Earth Systems*, *4*(2), M04001. https://doi.org/10.1029/2011MS000099

Reed, K. A., Medeiros, B., Bacmeister, J. T., & Lauritzen, P. H. (2015). Global radiative–convective equilibrium in the Community Atmosphere Model, version 5. *Journal of the Atmospheric Sciences*, *72*(5), 2183–2197. https://doi.org/10.1175/JAS-D-14-0268.1

Reed, K. A., Stansfield, A. M., Wehner, M. F., & Zarzycki, C. M. (2020). Forecasted attribution of the human influence on Hurricane Florence. *Science Advances*, *6*. https://doi.org/10.1126/sciadv.aaw9253

Reed, K. A., Wehner, M. F., Stansfield, A. M., & Zarzycki, C. M. (2021). Anthropogenic influence on Hurricane Dorian's extreme rainfall. *Bulletin of the American Meteorological Society*, *102*(1), S9–S15. https://doi.org/10.1175/BAMS-D-20-0160.1

Rios Gaona, M. F., Villarini, G., Zhang, W., & Vecchi, G. A. (2018). The added value of imerg in characterizing rainfall in tropical cyclones. *Atmospheric Research*, *209*, 95–102. https://doi.org/10.1016/j.atmosres.2018.03.008

Risser, M. D., & Wehner, M. F. (2017). Attributable human-induced changes in the likelihood and magnitude of the observed extreme precipitation during Hurricane Harvey. *Geophysical Research Letters*, *44*(24), 12–457. https://doi.org/10.1002/2017GL075888

Romps, D. M. (2011). Response of tropical precipitation to global warming. *Journal of the Atmospheric Sciences*, *68*(1), 123–138. https://doi.org/10.1175/2010JAS3542.1

Seeley, J. T., & Romps, D. M. (2015). Why does tropical convective available potential energy (CAPE) increase with warming? *Geophysical Research Letters*, *42*(2310), 10429–10437. https://doi.org/10.1002/2015GL066199

Shaevitz, D. A., Camargo, S. J., Sobel, A. H., Jonas, J. A., Kim, D., Kumar, A., et al. (2014). othersCharacteristics of tropical cyclones in high-resolution models in the present climate. *Journal of Advances in Modeling Earth Systems*, *6*(4), 1154–1172. https://doi.org/10.1002/2014MS000372

Shi, X., & Bretherton, C. S. (2014). Large-scale character of an atmosphere in rotating radiative-convective equilibrium. *Journal of Advances in Modeling Earth Systems*, *6*(3), 616–629. https://doi.org/10.1002/2014MS000342

Stansfield, A. M., & Reed, K. A. (2021). *CAM Global RCE simulations TC track, radial profiles, and filtered precipitation files*. Dryad. https://doi.org/10.5061/dryad.x3ffbg7jv

Stansfield, A. M., Reed, K. A., & Zarzycki, C. M. (2020). Changes in precipitation from north atlantic tropical cyclones under RCP scenarios in the variable-resolution community atmosphere model. *Geophysical Research Letters*, *47*(12), e2019GL086930. https://doi.org/10.1029/2019GL086930

Stansfield, A. M., Reed, K. A., Zarzycki, C. M., Ullrich, P. A., & Chavas, D. R. (2020). Assessing tropical cyclones' contribution to precipitation over the eastern united states and sensitivity to the variable-resolution domain extent. *Journal of Hydrometeorology*, *21*(7), 1425–1445. https://doi.org/10.1175/JHM-D-19-0240.1

Sun, Y., Zhong, Z., Li, T., Yi, L., Hu, Y., Wan, H., et al. (2017). Impact of ocean warming on tropical cyclone size and its destructiveness. *Scientific Reports*, *7*(1), 1–10. https://doi.org/10.1038/s41598-017-08533-6

Tang, B., & Emanuel, K. (2012). A ventilation index for tropical cyclones. *Bulletin of the American Meteorological Society*, *93*(12), 1901–1912. https://doi.org/10.1175/BAMS-D-11-00165.1

Taylor, M. A., & Fournier, A. (2010). A compatible and conservative spectral element method on unstructured grids. *Journal of Computational Physics*, *229*(17), 5879–5895. https://doi.org/10.1016/j.jcp.2010.04.008

Taylor, M. A., Tribbia, J., & Iskandarani, M. (1997). The spectral element method for the shallow water equations on the sphere. *Journal of Computational Physics*, *130*(1), 92–108. https://doi.org/10.1006/jcph.1996.5554

Tompkins, A. M., & Craig, G. C. (1999). Sensitivity of tropical convection to sea surface temperature in the absence of large-scale flow. *Journal of Climate*, *12*(2), 4622–476. https://doi.org/10.1175/1520-0442(1999)012<0462:sotcts>2.0.co;2

Trenberth, K. E., Cheng, L., Jacobs, P., Zhang, Y., & Fasullo, J. (2018). Hurricane Harvey links to ocean heat content and climate change adaptation. *Earth's Future*, *6*(5), 730–744. https://doi.org/10.1029/2018EF000825

Ullrich, P. A., & Zarzycki, C. M. (2017). TempestExtremes: A framework for scale scale-insensitive pointwise feature tracking on unstructured grids. *Geoscientific Model Development*, *10*, 1069–1090. https://doi.org/10.5194/gmd-10-1069-2017

Ullrich, P. A., Zarzycki, C. M., McClenny, E. E., Pinheiro, M. C., Stansfield, A. M., & Reed, K. A. (2021). Tempest extremes v2.0: A community framework for feature detection, tracking and analysis in large datasets. *Geoscientific Model Development*, *14*, 5023–5048. https://doi.org/10.5194/gmd-14-5023-2021

Van Oldenborgh, G. J., Van Der Wiel, K., Sebastian, A., Singh, R., Arrighi, J., Otto, F., et al. (2017). Attribution of extreme rainfall from Hurricane Harvey. *Environmental Research Letters*, *12*(12), 124009. https://doi.org/10.1088/1748-9326/aa9ef2

Vannière, B., Roberts, M., Vidale, P. L., Hodges, K., Demory, M.-E., Caron, L.-P., et al. (2020). The moisture budget of tropical cyclones in HighResMIP models: Large-scale environmental balance and sensitivity to horizontal resolution. *Journal of Climate*, *33*(19), 8457–8474. https://doi.org/10.1175/JCLI-D-19-0999.1

Villarini, G., Lavers, D. A., Scoccimarro, E., Zhao, M., Wehner, M. F., Vecchi, G. A., et al. (2014). Sensitivity of tropical cyclone rainfall to idealized global-scale forcings. *Journal of Climate*, *27*(12), 4622–4641. https://doi.org/10.1175/JCLI-D-13-00780.1

Walsh, K., Sharmila, S., Thatcher, M., Wales, S., Utembe, S., & Vaughan, A. (2020). Real world and tropical cyclone world. Part II: Sensitivity of tropical cyclone formation to uniform and meridionally varying sea surface temperatures under aquaplanet conditions. *Journal of Climate*, *33*(4), 1473–1486. https://doi.org/10.1175/JCLI-D-19-0079.1

Wang, S. S., Zhao, L., Yoon, J.-H., Klotzbach, P., & Gillies, R. R. (2018). Quantitative attribution of climate effects on Hurricane Harvey's extreme rainfall in Texas. *Environmental Research Letters*, *13*(5), 054014. https://doi.org/10.1088/1748-9326/aabb85

Wehner, M. F., Prabhat, Reed, K. A., Stone, D., Collins, W. D., Bacmeister, J., & Bacmeister, J. (2015). Resolution dependence of future tropical cyclone projections of CAM5.1 in the U.S. CLIVAR hurricane working group idealized configurations. *Journal of Climate*, *28*(10), 3905–3925. https://doi.org/10.1175/JCLI-D-14-00311.1

Wehner, M. F., Reed, K. A., Li, F., Bacmeister, J., Chen, C.-T., Paciorek, C., et al. (2014). The effect of horizontal resolution on simulation quality in the Community Atmospheric Model, CAM5.1. *Journal of Advances in Modeling Earth Systems*, *6*(4), 980–997. https://doi.org/10.1002/2013MS000276

Wehner, M. F., Reed, K. A., Loring, B., Stone, D., & Krishnan, H. (2018). Changes in tropical cyclones under stabilized 1.5 and 2.0°c global warming scenarios as simulated by the Community Atmospheric Model under the HAPPI protocols. *Earth System Dynamics*, *9*(1), 187–195. https://doi.org/10.5194/esd-9-187-2018

Wing, A. A., Camargo, S. J., & Sobel, A. H. (2016). Role of radiative–convective feedbacks in spontaneous tropical cyclogenesis in idealized numerical simulations. *Journal of the Atmospheric Sciences*, *73*(7), 2633–2642. https://doi.org/10.1175/JAS-D-15-0380.1

Wing, A. A., & Cronin, T. W. (2016). Self-aggregation of convection in long channel geometry. *Quarterly Journal of the Royal Meteorological Society*, *142*(694), 1–15. https://doi.org/10.1002/qj.2628

Wing, A. A., Emanuel, K. A., Holloway, C. E., & Muller, C. (2017). Convective self-aggregation in numerical simulations: A review. *Surveys in Geophysics*, *38*, 1173–1197. https://doi.org/10.1007/s10712-017-9408-4

Wing, A. A., Reed, K. A., Satoh, M., Stevens, B., Bony, S., & Ohno, T. (2018). Radiative-convective equilibrium model intercomparison project. *Geoscientific Model Development*, *11*, 793–813. https://doi.org/10.5194/gmd-11-793-2018

Wing, A. A., Stauffer, C. L., Becker, T., Reed, K. A., Ahn, M.-S., Arnold, N. P., et al. (2020). othersClouds and convective self-aggregation in a multimodel ensemble of radiative-convective equilibrium simulations. *Journal of Advances in Modeling Earth Systems*, *12*(9), e2020MS002138. https://doi.org/10.1029/2020MS002138

Wright, D. B., Knutson, T. R., & Smith, J. A. (2015). Regional climate model projections of rainfall from US landfalling tropical cyclones. *Climate Dynamics*, *45*(11–12), 3365–3379. https://doi.org/10.1007/s00382-015-2544-y

Zarzycki, C. M., & Jablonowski, C. (2014). A multidecadal simulation of Atlantic tropical cyclones using a variable-resolution global atmospheric general circulation model. *Journal of Advances in Modeling Earth Systems*, *6*(3), 805–828. https://doi.org/10.1002/2014MS000352

Zhou, W., Held, I. M., & Garner, S. T. (2014). Parameter study of tropical cyclones in rotating radiative–convective equilibrium with column physics and resolution of a 25-km GCM. *Journal of the Atmospheric Sciences*, *71*(3), 1058–1069. https://doi.org/10.1175/jas-d-13-0190.1